Article

Marine heatwaves suppress ocean circulation and large vortices in the Gulf of Alaska

Check for updates

Maya C. Rallu De Malibran ®, Chloe M. Kaplan® & Emanuele Di Lorenzo ® ✉

Large-scale anticyclonic vortices forming along the Gulf of Alaska continental slope serve as fertile ecosystems for marine life, significantly shaping the distribution of primary productivity, with 40–80% of the gulf's open ocean surface chlorophyll-a concentrated in their cores. Between 2013 and 2023, Alaska experienced some of the largest and longest marine heatwaves ever recorded in the world's oceans, persistently altering its ecosystem and fisheries. Here, using 30 years of satellite and reanalysis data, we find that the coastal upwelling atmospheric forcing conditions associated with the heatwaves have also significantly suppressed the Gulf of Alaska's ocean circulation and the formation of large anticyclones. Climate model simulations spanning from 1850 to 2100 suggest that future changes in the Aleutian Low pressure system will lead to a 60% increase in upwelling extremes (>2 standard deviations), further weakening the ocean anticyclones. However, large uncertainties remain in the mechanisms controlling the Aleutian Low's response to climate forcing in the models.

Recent climate extremes and trends in surface temperature and chlorophyll-a have significantly impacted the functioning of the Gulf of Alaska (GOA) marine ecosystem across multiple trophic levels. From 2013 to 2023, the Northeast Pacific experienced some of the most extreme multi-year climate events in recorded history. This period includes the 2014–15 and 2019 marine heatwaves[1–3] and the 2016 El Niño event. These events are evident in the time series of sea surface temperature anomalies (SSTa) observed in the GOA (Fig. 1a), which shows several warm extremes superimposed on a warmer decadal mean state that may reflect long-term climate change (e.g., warming) or the region's strong decadal variability. Due to the large-scale footprint of these extremes (Fig. 1b) and their multi-year spatial and temporal evolution[4,5], the ecological impacts on both lower and higher trophic levels and commercial fisheries have been widespread throughout the Northeast Pacific. Notably, there have been massive die-offs of marine mammals and the closure of shellfish fisheries due to the onset of harmful algal blooms[6–11].

Significant changes in ecosystem functioning in the GOA, particularly in the lower trophic levels and zooplankton, have been linked to the 2014–2015 marine heatwave (MHW). This event has led to a shift towards species that thrive in warmer waters, impacting the food chain[12]. Analyses of time series data, ranging from primary production to commercial fisheries, indicate that the effects of the MHW in the GOA were still ongoing across various levels of the marine food web at least five years after the 2014–2015 MHW[13–15], including diverse responses among top predators[16]. These warm extremes are further exacerbated by acidification and low oxygen events[17]

and are projected to get worse[18], posing a significant challenge to the management of GOA marine ecosystems.

Mesoscale eddies have long been recognized as crucial in sustaining the GOA's ocean primary productivity by influencing the distribution and abundance of marine resources through the transport of nutrients and organisms[19,20]. Specifically, large anticyclonic eddies that form along the continental slope of the GOA are a primary mechanism for entraining and transporting limiting micronutrients, such as iron[21,22], from the shelf region into the high-nutrient, low-chlorophyll area, thus supporting GOA interior marine ecosystems[23,24]. This entrainment also concentrates phytoplankton and zooplankton biomass in the eddy's cores[25] and influences chlorophyll-a (CHL-a) distribution along the eastern and western GOA, south of the Aleutian Islands[20,26]. This is evident from the analysis of satellite sea surface height anomalies (SSHa) from 1993 to 2023, which shows that regions of high SSHa standard deviation along the continental slope of the GOA (Fig. 2e, indicating high eddy activity) are correlated with CHL-a distribution (Fig. 2f). The influence of eddies and their transport has also been reported on the distribution of zooplankton concentrations[27,28] and larval fish assemblages along the continental shelf and slope, which correlate with eddy activity[29]. As eddies enhance primary productivity, their effects have also been documented on marine mammals and seabirds[30–33].

While the GOA's eddy-scale circulation is crucial for understanding marine ecosystem variability and change, it remains uncertain how recent climatic extremes and trends are affecting coastal circulation and large anticyclonic eddies. Analyzing the average sea level pressure anomalies
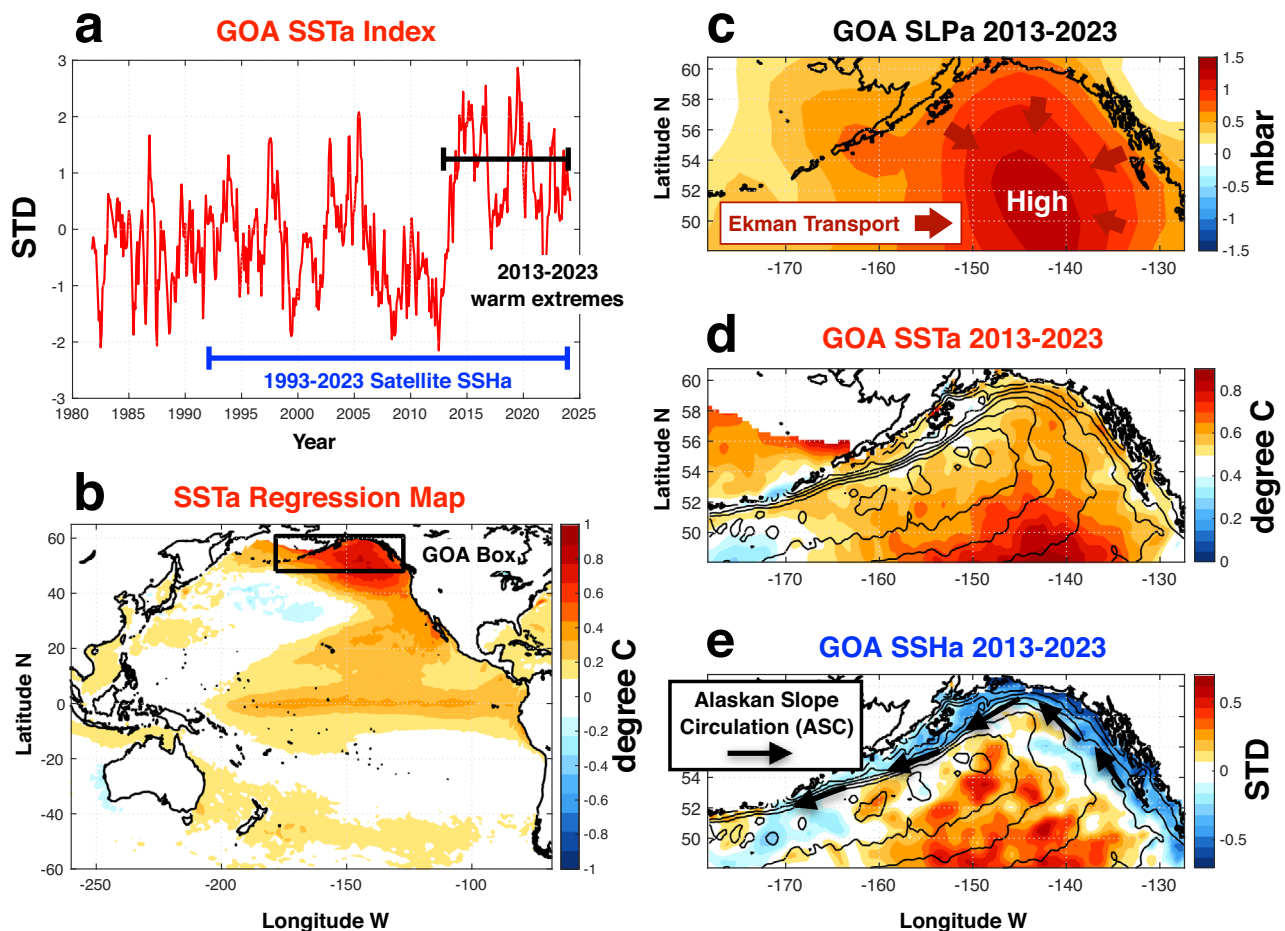
Department of Earth, Environmental, and Planetary Sciences, Brown University, Providence, RI, USA. ✉e-mail: e.dilorenzo@brown.edu

Fig. 1 | Recent warm extreme in the GOA. a Timeseries of GOA SSTa Index defined as the average SSTa in the black box region shown in (**b**), excluding the Bearing Sea anomalies. **b** Regression of Pacific SSTa with the GOA SSTa index. **c** Average anomalies of SLPa between 2013 and 2023 showing predominant coastal upwelling at the coast and downwelling in the GOA interior (red arrows show the direction of ocean Ekman transport). **d** Same as (**c**) but for SSTa, showing the core warming in the GOA interior. **e** Same as (**c**) but for SSHa, showing a weakening of the sea level gradient between the coast and the interior, which is indicative of a weaker ASC. The black contours show the path of the mean circulation from the satellite Mean Dynamic Topography (see "Methods") and the black arrows the location of the mean ASC, which tracks the Alaska Current and Alaskan Stream together.

(SLPa) during the period of the extremes 2013–2023 reveals a pattern (Fig. 1c) with higher than usual SLPa in the center of the GOA. This pattern favors a clockwise surface wind circulation that induces ocean transport (e.g., Ekman transport) away from the coast, resulting in coastal upwelling and offshore downwelling in the center of the GOA. This atmospheric pattern has been recognized as a driver of warm anomalies, shown in Fig. 1d, with a core of warmer water offshore relative to the coast[1,34]. While this SSTa pattern aligns with large-scale downwelling in the center of the GOA, a complete understanding of this structure requires considering additional ocean dynamics and surface heat fluxes. It should be noted that strong El Niño like the 1997–1998 and 2014–2015 are also linked to warming in the GOA. However, El Niño's atmospheric teleconnections drive stronger than usual coastal downwelling rather than upwelling, with the most significant warming occurring along the coastline (e.g., surface warm water converging at the coast).

From a dynamical perspective, both the upwelling forcing pattern (Fig. 1c) and thermal expansion of water (Fig. 1d, showing the warming) alter the gradient of SSHa, with high SSHa offshore in the core of the warming and downwelling, and lower SSHa along the coast linked to upwelling conditions. This response is evident in the SSHa observed from satellites between 2013 and 2023 (Fig. 1e). This SSHa pattern indicates a weaker Alaska Current and Alaskan Stream, which we will refer to as the Alaska Continental Slope Circulation (ASC). On the shelf region, the Alaskan Coastal Current is also influenced by significant freshwater runoff,

precipitation, and glacial that contribute to a lower salinity, buoyant coastal current that flows westward along the coast[35]. However, the freshwater effects are less significant for the continental slope circulation dynamics. In this paper, we investigate whether and how these atmospheric and thermal forcing patterns in the GOA have contributed to both the weakening of the ASC and the subsequent reduction in anticyclonic eddy activity. We also discuss projections from climate and earth system models to determine if these recent changes are indicative of future trends expected under global warming.

Results
To understand the eddy response to the anomalous atmospheric forcing between 2013 and 2023, it is instructive to review the seasonal dynamics of the GOA circulation and eddies (Fig. 2). During winter, from November to January, stronger downwelling atmospheric forcing significantly intensifies the coastal and continental slope circulation of the GOA, primarily the ASC[35]. This phenomenon is evident in Fig. 2a, which shows higher sea levels at the coast and lower sea levels offshore. Following these downwelling events, the eddy field becomes energized during the spring months along the continental slope (Fig. 2b), from February to May, primarily marked by the emergence of large anticyclonic eddies. The primary mechanisms for eddy formation in this region involve instabilities of the ASC along the western GOA (e.g., Alaskan Stream)[36], as well as the development of recurrent meanders anchored around topographic features (e.g., islands) along the
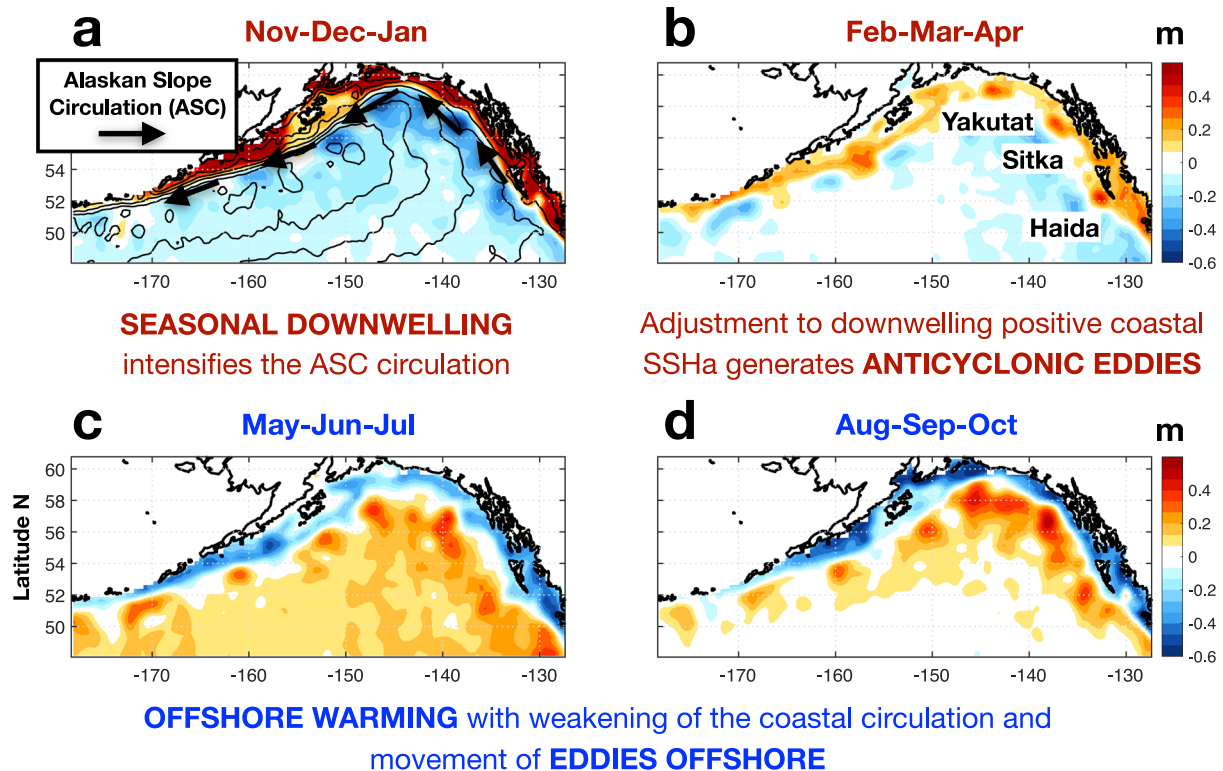
Fig. 2 | Seasonal and interannual variability of circulation and eddies in the GOA. Coastal circulation seasonal anomalies in SSHa for the periods Nov-Dec-Jan (**a**), Feb-Mar-Apr (**b**), May-Jun-Jul (**c**), and Aug-Sep-Oct (**d**) (units are in meters). **e** Interannual standard deviation of SSHa (units are in meters). In panel a, the black contours show the path of the mean circulation from the satellite Mean Dynamic Topography (see "Methods") and the black arrows the location of the mean ASC. **f** Point-wise correlation between interannual SSHa and CHL-a anomalies. The seasonal anomalies of SSHa are computed over the period 1993–2023 (see "Methods").

eastern basin, which then spin off as large anticyclonic eddies[37,38]. The large anticyclonic eddies that form through these geographically locked recurrent meanders in the eastern basin are referred to as the Haida, Sitka, and Yakutat eddies (Fig. 2b)[22,26,39,40].

During the transition towards summer, the warming leads to an overall increase in the SSH anomalies offshore (Fig. 2c). Concurrently, the eddies continue to move offshore and intensify, with a noticeable weakening in the ASC circulation (e.g., the seasonal SSHa coastal gradient is reversed). By the end of summer and the beginning of fall (Fig. 2d), the shelf circulation is at its weakest, and the eddies reach their maximum strength as they continue

their offshore trajectory. Notably, even at this stage, the distinct signatures of the Haida, Sitka, and Yakutat large anticyclonic eddies can still be tracked in their more distant offshore locations.

Given that the generation of eddies is linked to the intensification of the ASC following strong downwelling events[38], we begin by examining the long-term variability of the ASC during the period extremes 2013–2023. Figure 3a (blue line) displays the ASC Index, calculated by measuring the strength of the coastal gradient in SSHa along the GOA (see "Methods" for the exact definition). A correlation map between the ASC Index and SSHa (Fig. 3c) reveals a pattern of coherent positive SSHa along the entire coastal
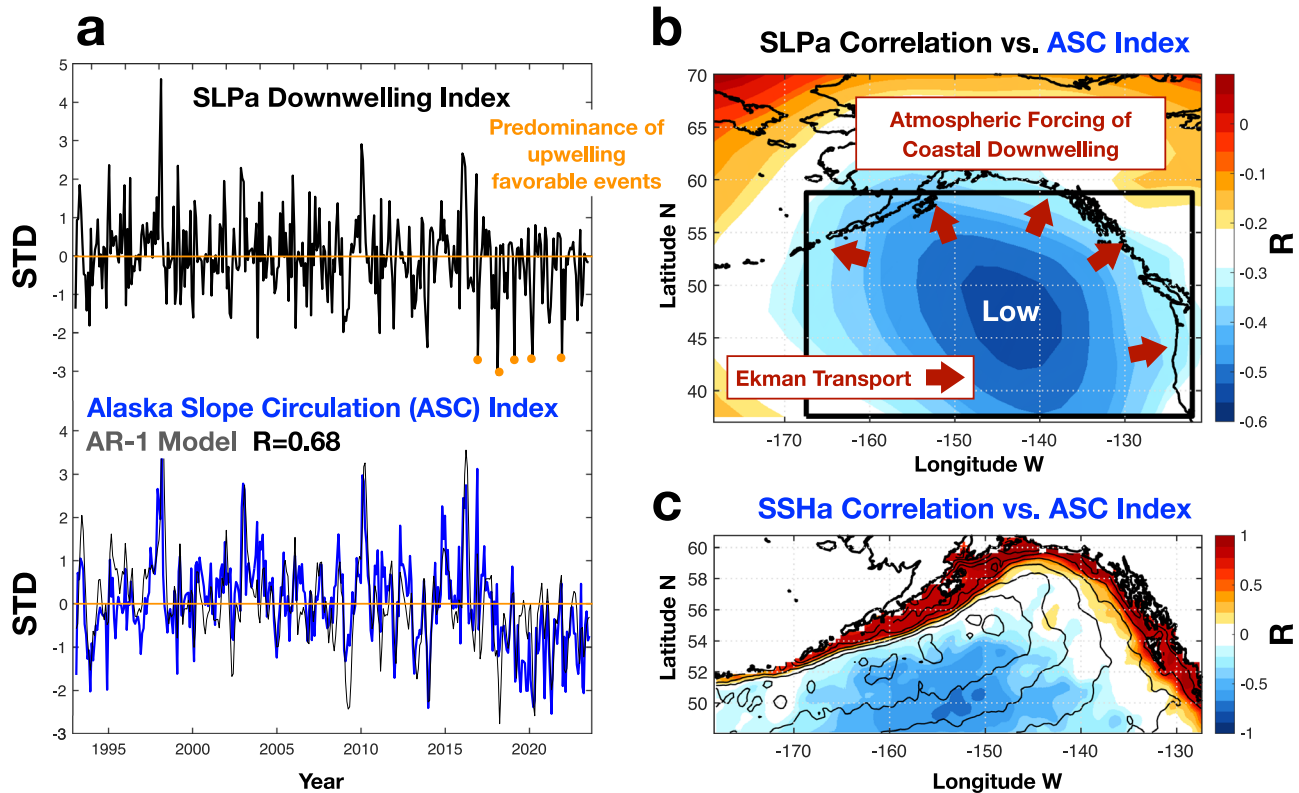
Fig. 3 | Analysis of coastal and atmospheric dynamics over the GOA. ((**a**), black line) Time series of SLPa Downwelling Index that measures the changes in the strength of the NCEP Reanalysis SLPa downwelling pattern shown in (**b**) (see "Methods"). ((**a**), blue line) Time series of ASC Index that measures the strength of the Alaska Current and Alaskan Stream along the continental slope regions of the GOA. The superimposed grey time series is the output of reconstructing the ASC Index using an AR-1 model forced by the SLPa Downwelling Index (see "Methods").

The reconstruction has a correlation skill of $R = 0.68$ (significant > 99%). **b** Correlation map of SLPa with the ASC Index showing the pattern of atmospheric forcing that drives coastal downwelling in the GOA (e.g., the red arrows show the direction of the Ekman transport towards the coast). **c** Correlation map of SSHa with the ASC Index showing that the index captures in its positive phase an intensification of the mean circulation along the coast with higher SSHa on the shelf.

GOA. This indicates that when the ASC Index is positive, the entire GOA experiences stronger than usual continental slope anti-clockwise circulation. The strong positive peaks observed in the ASC Index (Fig. 3a) are associated with the impacts of atmospheric winter teleconnections of El Niños, which produce stronger-than-usual downwelling events over the GOA. Over the period of the extremes 2013 to 2023, we also observe an overall reduction in the strength of the ASC Index starting after the strong 2015-2016 El Niño (Fig. 3a, blue line), with an anomalous period of negative values (weaker ASC). This reduction is linked to a predominance of upwelling events (Fig. 3a, orange dots) that generate lower sea levels along the Alaskan coast, a weaker ASC, and warming in the GOA interior (Fig. 1d).

To identify the pattern of atmospheric forcing that drives the variability of the ASC, we compute a correlation map of SLPa and the ASC Index (Fig. 3b). This map shows a strong negative pressure anomaly in the center of the GOA, associated with stronger than usual coastal downwelling conditions (Fig. 3b, see Ekman Transport arrows). This SLPa pattern is consistent with the seasonal downwelling pattern in winter and is the primary driver that energizes the ASC and the subsequent generation of eddies[41]. We now measure how the strength of the SLPa forcing pattern (Fig. 3b) changes over time by projecting the pattern onto the SLPa to derive the SLPa Downwelling Index (Fig. 3a, black line) (see "Methods"). Consistent with the observed weakening of the ASC index between 2013 and 2023, we find a series of strong upwelling forcing events (Fig. 3a, black line and orange dots), especially after the 2015–2016 El Niño. We then quantify how much of the ASC Index can be explained by a simple AR-1 model of coastal SSHa forced by the SLPa Downwelling Index (see "Methods" section on the coastal wind model). We find that the AR-1 model reconstruction has a significant correlation skill ($R = 0.68$, >99% significance) (see "Methods"

for significance test), confirming that a large fraction of the historical variations in coastal circulation, including the weakening after 2013, are linked to changes in downwelling atmospheric forcing.

We now examine how changes in the ASC and downwelling have impacted the large eddies in the GOA. To this end, it is informative to closely analyze the response of eddies to strong downwelling and upwelling events at the interannual timescale. Figure 4a shows all occurrences when the SLPa Downwelling Index is larger than 1 STD (red lines, downwelling events) and smaller than -1 STD (blue lines, upwelling events). An example of the SSHa evolution (Fig. 5a) during the strongest downwelling event on record, which occurred in the winter of 1998 during El Niño[42] (marked with a black dot in Fig. 4a), clearly shows the development of strong eddies, particularly the recurrent Haida, Sitka, and Yakutat eddies. In contrast, we find no trace of eddy formation when we compare this evolution with that of the SSHa during the strongest upwelling event in the winter of 2018 (Fig. 5b). This behavior is also evident in composite SSHa anomalies for strong downwelling and upwelling events (not shown). Shifting our focus back to the downwelling extremes in the SLP Downwelling Index (Fig. 4a), we find a complete disappearance of downwelling events with STD > 1 after the El Niño of 2015–2016 and a prominent emergence of stronger than usual upwelling events (Fig. 4a, blue lines). This shift in wind statistics is unprecedented in the SSHa satellite record period between 1993-present.

To conduct a more comprehensive assessment of how the predominance of upwelling events between 2013 and 2023 may have suppressed the activity of large anticyclones in the GOA, we developed several measures of eddy activity (see "Methods"). We begin by counting the transit of large eddies at each location by counting the number of times SSHa has an amplitude above 0.15 m (see "Methods"). The threshold of 0.15 m is
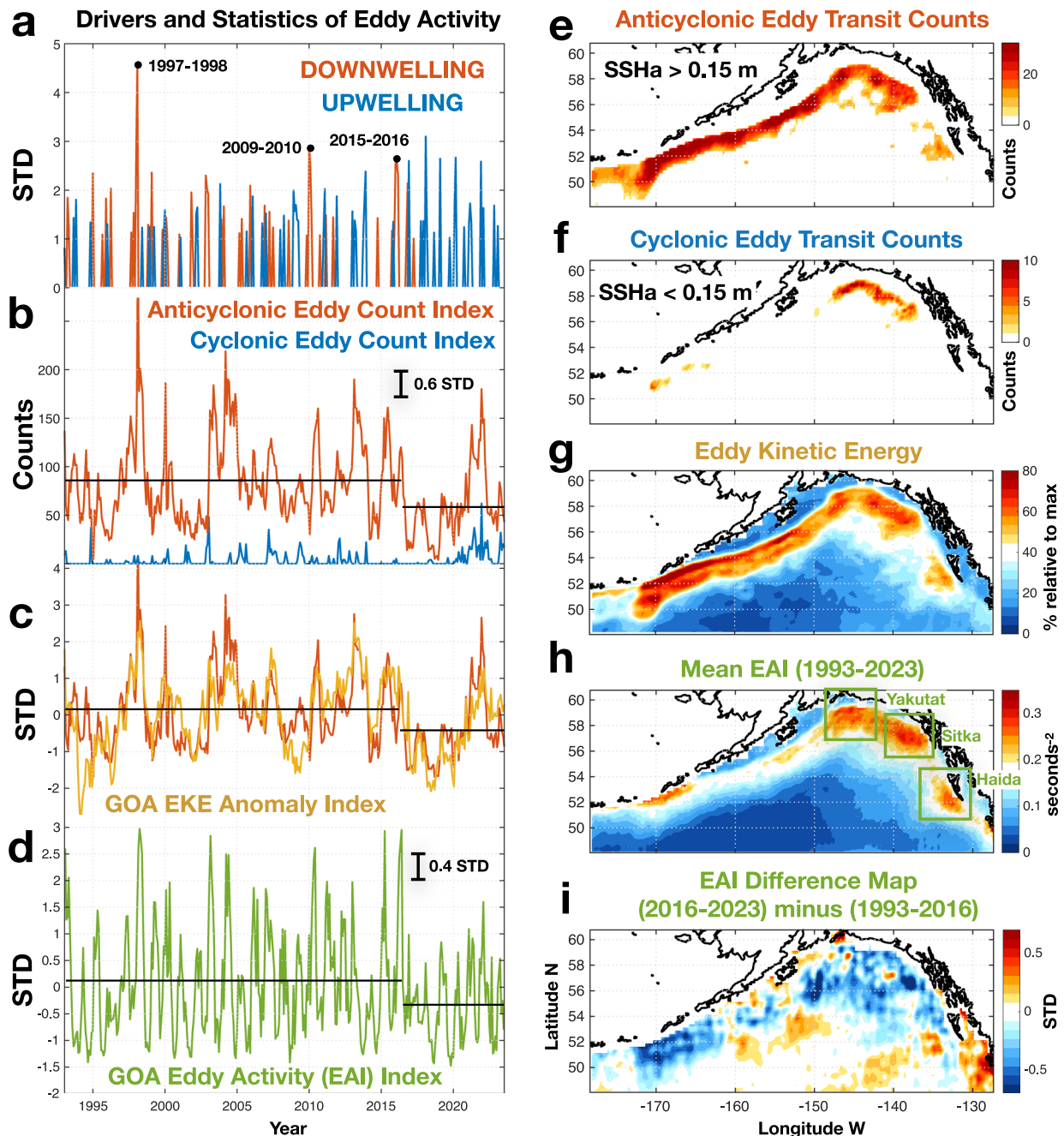
Fig. 4 | Drivers and statistics of eddy activity. a Time series of coastal upwelling and downwelling events when the SLPa Downwelling Index (Fig. 2a) exceeds 1 STD. **b** Anticyclonic and cyclonic eddy count indices for each SSHa time record, defined by the number of pixels in sea surface height anomalies (SSHa) that exceed 3 STDs (0.15 m). **c** Normalized anticyclonic eddy count index is compared with GOA interior mean EKE anomalies (yellow line, *R* = 0.7). **d** Eddy Activity Index (EAI) (green line). The black line in (**b**–**d**) represents the mean of the indices before and after the 2015–2016 El Niño event, highlighting a significant reduction of 0.6 STD (99% significance) in the anticyclonic eddy count index and a 0.4 STD (99%

significance) reduction in the EAI (see "Methods"). **e, f** show anticyclonic and cyclonic eddy transit counts, respectively, defined as the number of pixels experiencing SSHa greater than 0.15 m (3 STD) and less than −0.15 m (3 STD). **g** Mean EKE in the GOA as a percentage of the maximum EKE recorded, computed as a time-averaged EKE over 1993–2023, with both SSHa and EKE derived from the same satellite-merged dataset. **h** Mean of EAI computed over the period 1993–2023. **i** Difference map in the mean EAI between the periods before and after the 2015–2016 El Niño event, with the map rescaled by the STD of the EAI so that units of change are in STD (1 STD = 0.07 s^{-2}).

equivalent to 3 STD of the SSHa. Comparing the eddy transit count of anticyclonic versus cyclonic eddies (Fig. 4e and f), we find that the GOA eddy field is dominated by stronger anticyclones. As expected, the pattern of anticyclonic eddy counts closely tracks the pattern of mean eddy kinetic energy in the GOA interior (Fig. 4g). The temporal indices of eddy counts, shown in Fig. 4b, measure the total number of large anticyclones (red line) and cyclones (blue line) for a given time record of SSHa by counting the number of pixels exceeding the ±3 STD threshold (see "Methods").

Consistent with the eddy count maps, the anticyclonic eddy count index is significantly larger than the cyclonic eddy index (Fig. 4b). However, between 2013 and 2023, there is an overall reduction in anticyclonic eddy count compared to the rest of the observational satellite record. While low values of the anticyclonic eddy index appear in other parts of the timeseries, the sustained period of lower index values (0.6 STD) after the 2015–2016 El Nino is significant at the 99% confidence level (see "Methods" for description of significance test). Concurrently, over this period, there is a
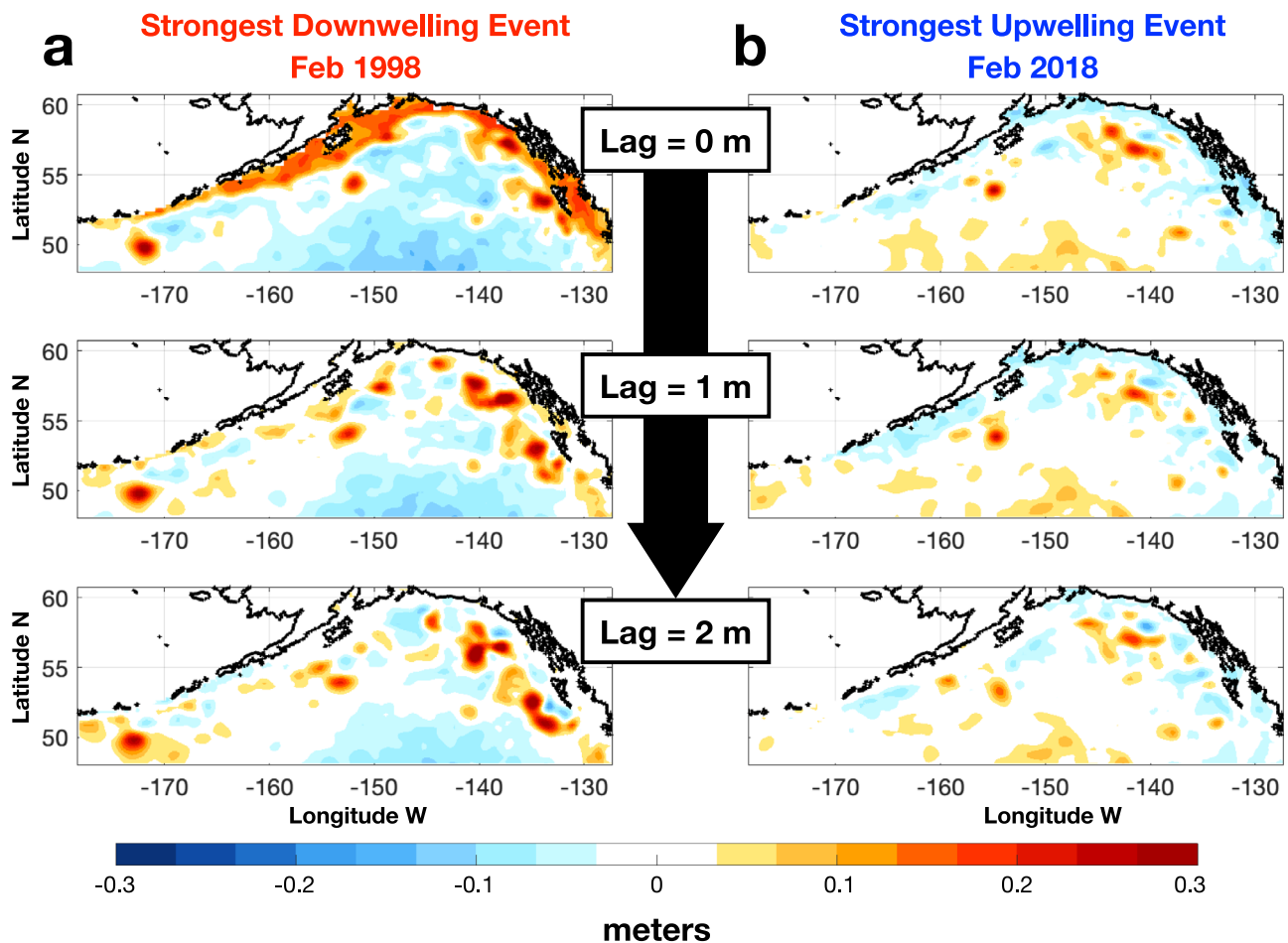
Fig. 5 | Examples of eddy response to strong downwelling and upwelling conditions. a SSHa from Feb 1998 to April 1998 associated with the strongest downwelling event on record during the El Niño winter of 1998 when the SLPa Downwelling Index > 4 STD. **b** SSHa from Feb 2018 to April 2018 associated with the strongest winter upwelling event on record when the SLPa Downwelling Index < −3.

notable increase in the cyclonic eddy count index, which is substantial compared to historical variability and likely linked to the predominance of upwelling events. We further compare the anticyclonic eddy index with a timeseries of the average eddy kinetic energy (EKE) over the GOA (Fig. 4c, yellow line) to verify how well our index of anticyclonic eddy activity tracks an independent measure of eddy variability. The strong correlation between these two indices ($R = 0.7 > 99\%$ significance) confirms again that anticyclonic eddies dominate the EKE in the GOA as suggested by the spatial correspondence between the maps of anticyclonic eddy count (Fig. 4g) and EKE (Fig. 4e).

Lastly, we examine the Eddy activity index (EAI) to estimate the growth and decay of eddies. Defined as the absolute value of the time derivative of relative vorticity, the EAI provides a dynamic measure of eddy generation and dissipation within the region. The long-term mean of the EAI, computed at each pixel (Fig. 4h), exhibits a pattern similar to that of eddy kinetic energy (Fig. 4g), though areas of elevated EAI are more concentrated in well-known eddy generation sites, such as the Haida, Sitka, and Yakutat regions, where large anticyclones frequently form. The fact that the EAI peaks in these key eddy generation regions reinforces our confidence that this index effectively tracks the formation of eddies. The EAI also enables the creation of a time series to track the intense eddy activity (EAI > 3 STD) over time (Fig. 4d, green line) (see "Methods"). In alignment with eddy count indices, the EAI time series (Fig. 4d) shows a marked suppression following the 2015–2016 El Niño, characterized by a distinct decline in both variability and overall activity levels compared to the pre-El Niño period. This is reflected in the significantly lower standard deviations (−0.4 STD; 99% significance) in the years after the event. Figure 4i further highlights the

spatial distribution of these changes, with the EAI difference map showing a significant reduction in eddy activity across much of the GOA, particularly in the central and western regions, following the 2015–2016 El Niño when the GOA experienced the succession of upwelling events (Fig. 4a, blue line).

Discussion

The analysis of satellite SSHa demonstrates that the anomalous atmospheric forcing of the MHWs affecting the GOA ecosystem from 2013 to 2024 has led to a suppression of strong downwelling events (<1 STD in the SLPa Downwelling Index, Fig. 4a), particularly after the winter of the 2015–2016 El Niño. The ocean circulation response to these forcings has resulted in a general weakening of the Alaska shelf coastal circulation (Fig. 3a) and a significant reduction in the activity of large anticyclonic eddies (Fig. 4b–d). These eddies dominate the mesoscale transport of ocean tracers in the region, such as nutrients, phytoplankton, and zooplankton, and their amplitude and lifetime are greater than those of cyclones[43] (see also discussion of Fig. 4). While we cannot fully quantify the biological significance of these changes on the GOA marine ecosystem, Crawford et al. [44] highlighted that 40–80% of all surface chlorophyll in the GOA interior (waters deeper than 500 m) is concentrated within large anticyclonic eddies, despite these eddies occupying only 10% of the total surface area. Although Crawford et al. did not assess subsurface chlorophyll—which is likely substantial due to the presence of a deep chlorophyll maximum—a proportional relationship between surface and deep chlorophyll within these eddies is probable. Supporting this, Ladd et al. [22] documented subsurface maxima in iron within the eddy cores, which can stimulate phytoplankton production. However, this relationship is not universally consistent across

different regions and conditions, suggesting that local variability plays a significant role. Additionally, extensive research has shown how anticyclones impact all trophic levels of the GOA marine food web[20]. By documenting the relationship between MHWs and eddies in the GOA, our findings provide new insights into the dynamic pathways that link climate forcing, changes in ocean transport processes, and the responses of marine ecosystems to climate extremes. While MHWs and changes in eddies may co-occur in response to the same atmospheric drivers, their impacts on ecosystems unfold through different pathways, with MHWs primarily affecting marine life via direct temperature-mediated effects. In contrast, eddies influence ecosystem dynamics through changes in nutrient transport, water column stratification, and biogeochemical processes. This distinction underscores the complex and multifaceted nature of how climate extremes influence marine ecosystems.

The decrease in eddy activity found in this study offers a complementary regional perspective to other global studies, which report that mesoscale eddy variability (e.g., EKE) has increased by 2–5% in eddy-rich regions, such as the higher latitudes where the western boundary currents are located[45], and is projected to intensify further and shift poleward in the Kuroshio[46]. Specifically, our study highlights that although the maximum amplitude of Alaskan eddies may not match that of those in the western boundary currents, their biological impact is equally profound in terms of altering ecosystem functions. This suggests that linking trends in eddy variability to changes in the marine ecosystem on a global scale may require more nuanced regional interpretations such as the one provided in this study. The global scope of previous studies on eddy statistics and climate change makes it difficult to conclusively determine if the observed reduction in anticyclonic eddies in the GOA from 2013 to 2023 indicates changing conditions. However, it is theoretically possible to project future changes by exploiting the mechanistic link between the ASC, the generation of eddies, and their atmospheric forcing pattern (e.g., Fig. 1c), which in this region reflects changes in the Aleutian Low (AL)—the dominant pattern of atmospheric variability in this region.

Despite the large internal variability that climate models exhibit over North America[47], recent studies report that extreme events associated with the AL are projected to increase[48] with a northward expansion and intensification of the AL center of action[49,50]. From a large-scale perspective, these projected changes in the AL would lead to a stronger SLP low over the North Pacific, which at first glance would be indicative of stronger coastal downwelling in the GOA and stronger anticyclonic eddy activity. This would imply that recent upwelling extremes and the reduction of large anticyclones reported in this study are part of natural variability. However, to understand the impact of downwelling and upwelling, one must carefully consider the geographic projections of AL changes over the GOA coastal region. For example, the shifts and intensification of the AL reported by Gan et al. (2017, their Fig. 3d)[49] show a pattern of SLPa change that is difficult to interpret in the context of upwelling and downwelling over the GOA shelf.

To better understand the significance of AL changes for GOA eddies, we use the same models as Gan et al.[49] from CMIP6 and examine how changes in the AL project onto upwelling and downwelling atmospheric events over the GOA shell in future climates. We analyze SLPa in 27 models from the CMIP6 archive over the period 1850–2100, which includes both historical and SSP585 future projected scenarios (see "Methods"). For each model, we compute their normalized SLPa Downwelling Index by projecting the observed atmospheric downwelling forcing patterns inferred from the reanalysis product (Fig. 3b) (see "Methods"). The probability distribution function (PDF) of the downwelling indices from all models is shown in Fig. 6a, comparing the period 1850–1950 (blue line) with the period 2000–2100 (red line) (see "Methods" for the computation of the PDF). Positive values in the PDF indicate downwelling events, whereas negative values indicate upwelling events. We then calculate and plot the differences between the PDFs by subtracting the historical PDF from the future PDF (Fig. 6b). Our results show a significant increase in upwelling events, including those that occur at -2 and -3 STD (see "Methods" for

significance test). For downwelling events, we observe an overall decrease in low-magnitude events, with the largest difference around 0.1 STD, indicating a small but significant trend in reduced downwelling. Additionally, we find an increase in downwelling extremes above 2 STD. Exploring these differences in terms of percentage change (Fig. 6c), we find that upwelling extremes (above 2 STD, Fig. 5c blue area) increase on average by 60%, while downwelling extremes (above 2 STD, Fig. 6c red area) increase by 20%. Taken together, the model projections suggest that upwelling extremes will increase significantly more than downwelling by a factor of 3. To understand how the small but significant negative trend in the SLP Downwelling Index impacts the PDF, we repeat the same analysis by removing the linear trend from the data (Fig. 6, right column) (see "Methods"). After detrending the data, we find that the changes in upwelling and downwelling extremes are comparable, both increasing by 50%. This indicates that the prominent increase in upwelling over downwelling events is linked to the trend.

While our analysis of the CMIP6 models provides some additional insight into how future changes in AL are projected to impact the GOA, the lack of consensus on key mechanisms and their representation in models makes these predictions remain uncertain. Dynamically, changes in the AL have been linked to shifts in both ENSO teleconnections[49] and Arctic Amplification (AA)[50]. Recent studies suggest that AA is impacting the statistics of mid-latitude extreme events and the position of the storm tracks[51]. These shifts in storm tracks are often reflected in changes in large-scale atmospheric modes[52], such as the position and strength of the Aleutian Low and its downwelling influence in the GOA. Other studies have linked Arctic warming to an increase in Northeast Pacific marine heatwave days during boreal summers[53]. However, while some studies suggest that AA may lead to a stronger winter Aleutian Low[50], others suggest the opposite, and overall, the debate about the role of AA on future changes in the Aleutian Low remains unclear[54–56]. Finally, it is worth noticing that both pathways, AA and ENSO teleconnections, to AL climate change remain still highly debated in the literature and with contradictory results, partly because projection models may not well represent the essential processes and patterns of ENSO teleconnections over the North Pacific[57].

Methods
Observational datasets
The eddy variability in the GOA is examined through satellite SSH and surface geostrophic currents data from the Global Ocean Gridded L 4 Sea Surface Heights by Copernicus Marine Data (https://doi.org/10.48670/moi-00148). The data are at monthly temporal resolution and with a horizontal average resolution of 0.25 degrees in longitude and in latitude over the Gulf of Alaska region. Climatological monthly averages are computed over the period 1993-2023 and removed to define the SSH anomalies (SSHa). For each timemap of SSHa, the domain average SSHa is removed as a constant. We also use the Mean Dynamic Ocean Topography (Release May 29, 2015) from the Asia–Pacific Data-Research Center between 1993 and 2023 to draw the contours of the mean SSH shown in the figures (http://apdrc.soest.hawaii.edu/datadoc/mdot.php).

Additionally, monthly means of Sea Surface Temperature (SST) are obtained from the National Oceanic and Atmospheric Administration/National Centers for Environmental Information 1/4 Degree Daily Optimum Interpolation Sea Surface Temperature Analysis, Version 2.1, between 1982 and 2023. We also use sea level pressure (SLP) data from the 'NCEP-NCAR Reanalysis 1 at monthly resolution and with a horizontal resolution of 2.5 degrees[58]. Interannual anomalies are derived by subtracting the climatological monthly mean computed over the same period of the SSHa between 1993 and 2023.

To understand the relation between physical and biological variability, we used monthly satellite observations of chlorophyll-a from the Ocean Color CCI Level-3 from 1997-2023[59] at monthly temporal resolution and with a horizontal average resolution of 2 km in longitude and 4 km in latitude over the Gulf of Alaska region. Data was downloaded from https://www.oceancolour.org/.
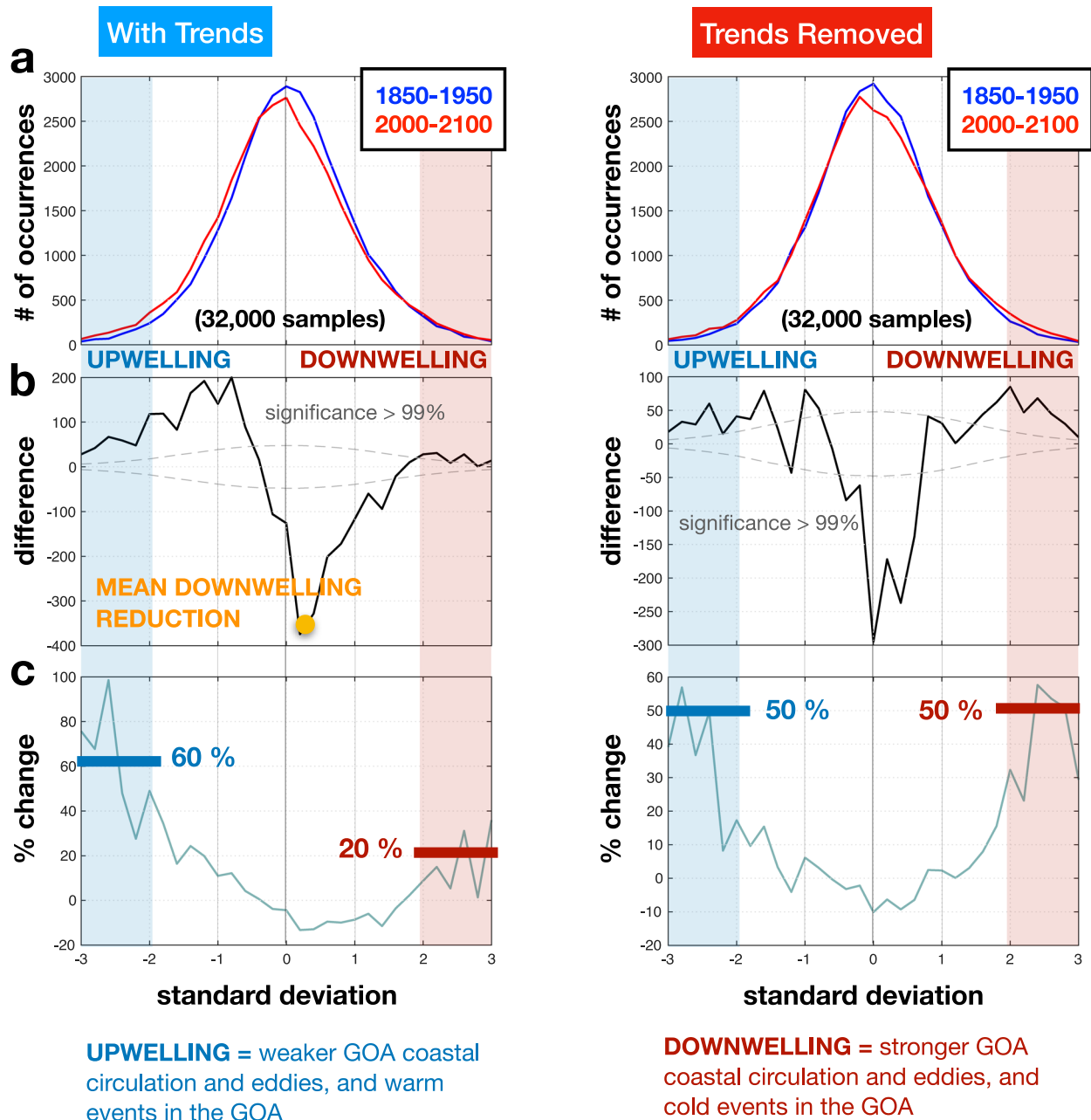
Fig. 6 | CMIP6 projections of downwelling and upwelling conditions in future climate. a PDF of SLPa Downwelling Index over the coastal GOA from 27 CMIP models for the historical period 1850-1950 (blue) vs. warming period 2000–2100 (red, under the SSP585 scenario) (see "Methods" for calculations). The x-axis is in units of standard deviation (STD) and the y-axis is the number of events in each bin. Each PDF has a total of 32,000 samples. **b** Difference in the PDFs 2000–2100 minus 1850–1950. The dotted lines show the 99% significance levels estimated using a Montecarlo Simulation with 10,000 samples (see "Methods"). **c** The difference plot of panel b is presented as a % change from the period 1850–1950 to 2000–2100, with positive values indicating an increase in events with a certain magnitude in units of STD. Note that events at the 2 STD and 3 STD represent extremes with probabilities of 5% and 1%. The left column presents the analysis where trends in the SLPa Downwelling indices have been retained, while in the right column linear trends have been removed prior to the PDFs calculations.

Alaska Continental Slope Circulation (ASC) index and wind model reconstruction

The ASC index. Interannual anomalies in the intensity of the coastal and continental slope circulation of the GOA are quantified by defining an ASC Index (Fig. 3a, blue line). This index measures the difference between the average SSHa over the shelf region (see Fig. 4d, blue region mask) and the average SSHa in the basin's offshore water (see Fig. 4d, red region mask) for each monthly satellite SSHa map. The shelf mask was obtained by computing correlation maps between SSHa and several timeseries of SSHa along the shelf. These correlation maps consistently showed high correlation over the shelf. By averaging these maps and setting a correlation threshold of R > 0.7, we identified the pixels corresponding to the shelf region. The ASC Index is normalized, and its values are in standard deviation units.

SLPa Downwelling Forcing Pattern and index. We first derive the optimal SLPa atmospheric forcing pattern that drives the ASC Index variability by correlating the ASC Index with SLPa (Fig. 3b). By projecting this pattern onto the time-dependent SLPa, we derive a timeseries of how the intensity of this pattern changes over time. We refer to this timeseries as the SLPa Downwelling Index (Fig. 3a, black line) because the SLPa pattern is linked to coastal downwelling winds, which are known to increase the strength of the ASC (Stabeno et al., 2004).

The wind reconstruction model. After normalizing the SLPa Downwelling Index by its standard deviation, we use it to reconstruct the ASC Index using a simple auto-regressive model of order one (AR-1):

$$\frac{dASCIndex(t)}{dt} = SLPaDownwellingIndex(t) - \gamma \cdot ASCIndex(t) \quad (1)$$

In this model, the rate of change of the ASC Index is forced by the SLPa Downwelling Index. Given that the coastal upwelling of SSHa has memory and the dissipation of the anomalies is linked to the development and offshore propagation of the eddies (with a timescale of approximately ~2 months), we also introduce a damping rate term on the right-hand side $\gamma = 1/2 months$. This type of AR-1 model has been used in previous studies to reconstruct the oceanic variability of upwelling and downwelling in the GOA[60] and in the reconstruction of large-scale SST anomalies in the Northeast Pacific[19,61–63]. The reconstructed ASC Index is then normalized by its standard deviation and compared to the original ASC Index (Fig. 3a, gray line for the reconstruction vs. blue line for the original). The reconstructed ASC Index from the AR-1 SLPa model has a significant correlation with the ASC Index computed from the SSHa data ($R = 0.68$).

Eddy indices and statistics
Anticyclonic and cyclonic eddy transits count. In this study, instead of tracking individual eddies in a Lagrangian framework (which follows eddies over time and space), we quantify the frequency of eddy transits using an Eulerian framework. Specifically, we count the number of times a large eddy passes through each pixel location in the satellite-derived SSHa data. We define large eddies as those with SSHa greater than 0.15 m. This threshold corresponds to 3 standard deviations above the mean SSHa, as determined from a histogram of all available SSHa data from 1993 to 2023. To ensure that this threshold is robust for capturing significant eddy activity, we also conducted a visual inspection of several strong downwelling events, such as those occurring during El Niño phases. These inspections confirmed that the 0.15 m threshold is effective for identifying large eddies (an example of which is shown in Fig. 5). For each SSHa 2D image, we count how many times a given pixel location experiences positive (anticyclonic) or negative (cyclonic) anomalies above this threshold. These counts are then summed over the period from 1993 to 2023 at each pixel, resulting in the eddy transit count maps shown in Fig. 4e and f. It is important to note that because the same eddy can contribute to the counts at multiple locations as it moves through the region, the "transit count" should be interpreted as the number of times a given location experiences the passage of a large eddy, rather than the total number of distinct eddies in the region.

Anticyclonic and cyclonic eddy count indices. To track the temporal changes in the number of large eddies present in the GOA at any given time, we develop anticyclonic and cyclonic eddy count indices using a similar approach to the eddy transit count. For each monthly map of SSHa, we calculate the total number of pixels with anomalies exceeding +3 STD for the anticyclonic eddy count index and below −3 STD for the cyclonic eddy count index (Fig. 4b). While these indices do not identify individual eddies, they provide a measure of how many pixels within the GOA domain are associated with large eddies at any given time, offering insight into the spatial extent of eddy activity.

Eddy activity index (EAI). To further quantify the eddy activity in the GOA, we also developed the Eddy activity index (EAI), which is based on the time derivative of relative vorticity derived from satellite-observed surface geostrophic currents. The process involves calculating the relative vorticity for each satellite record, followed by computing its time derivative and taking the absolute value to generate an EAI timeseries at each grid point. The EAI has units of relative vorticity over time (seconds^{-2}). To capture significant eddy growth and decay (Fig. 4d, green line), we spatially average all EAI values exceeding 3 STD for each time record. This resulting time series is then normalized by subtracting the mean and dividing by the standard deviation, ensuring that units of change are expressed in STD. The EAI provides a more dynamic measure of eddy generation and dissipation in the GOA, effectively tracking the intensity of eddy activity over time.

Significance test for correlations and changes in mean
To estimate the significance of correlations between two-time series, we used Monte Carlo simulations to account for the auto-correlation in the data. Here's the process:

- *Generating random time series*: We generate 10,000 random pairs of red noise time series with an STD of 1 that match the auto-regressive memory of the original time series.
- *Estimating correlations*: We compute the correlations between these random pairs to estimate the distribution of random correlations.
- *Confidence intervals*: We estimate the 95% and 99% confidence intervals for the correlations using this distribution.

We use a similar Monte Carlo simulation approach to examine the significance of changes in the mean of the Anticyclonic Eddy Activity Index (Fig. 4b, red line) between periods 2013–2023 and 1993–2013. The process involves the following steps:

- *Generating random time series*: First, we generate 10,000 random realizations of red noise time series that match the auto-regressive memory of the original time series with an STD of 1.
- *Computing mean differences*: For each realization, we compute the difference in means between the two periods in units of STD to build a distribution of random mean differences.
- *Establishing confidence intervals*: We determine the 95% and 99% confidence intervals for the mean differences from this distribution.

Analysis of climate and Earth system models simulations
CMIP6 data archive. We use the SLP output of 27 climate and earth system model simulations from the Coupled Model Intercomparison Project version 6 (CMIP6) to examine projected changes in the non-seasonal downwelling and upwelling atmospheric conditions. The data was downloaded from the Program for Climate Model Diagnosis & Intercomparison (PCMDI; https://pcmdi.llnl.gov). These include: ACCESS-CM2, BCC-CSM2-MR, CAMS-CSM1-0, CMCC-CM2-SR5, E3SM-1-0, E3SM-1-1, IITM-ESM, INM-CM5-0, KACE-1-0-G, MIROC6, MPI-ESM1-2-HR, MPI-ESM1-2-LR, NorESM2-LM, ACCESS-ESM1-5, CESM2-WACCM, CMCC-ESM2, CanESM5-1, CanESM5, E3SM-1-1-ECA, EC-Earth3-Veg-LR, FIO-ESM-2-0, IPSL-CM6A-LR, KIOST-ESM, MCM-UA-1-0, MRI-ESM2-0, NorESM2-MM, and TaiESM1. For each model, the monthly mean SLP from 1850-2100 was concatenated between the historical and future projection period under the Shared Socio-economic Pathway 585 (SSP585) used by the Intergovernmental Panel on Climate Change (IPCC). For each model, we picked only one ensemble member. The SSP585 represents a pathway where the world follows a trajectory of high greenhouse gas emissions due to an energy-intensive and fossil-fuel-driven economy[64]. Sea level pressure anomalies in each model were derived by removing the monthly climatology computed over the entire 1850-2100 period to retain the forced climate change signals.

Probability distribution functions (PDFs) of SLPa Downwelling index.
After computing the SLPa in each CMIP6 model, we use the same GOA

SLPa downwelling forcing pattern defined in Fig. 3b to extract the normalized SLPa Downwelling Index (same as in the "Method" section "*SLPa Downwelling Forcing Pattern and Index*"). After compiling the indices from each model, we combine all indices data to compute a PDF of the Downwelling Indices for two 100-year-long periods: 1850–1950 (Fig. 5a, blue line) and 2000–2100 (Fig. 5a, red line). The units on the x-axis (Fig. 5) are in standard deviations to highlight the regions where the downwelling index shows extreme events (e.g., standard deviation > 2). Negative values represent upwelling events when the sign's SLPa forcing pattern is reversed. These periods are selected to represent "normal conditions" before greenhouse gases began to have a significant impact on global temperatures (1850-1950) and "warming conditions" (2000–2100) when global temperatures are rising, and the external forcing of greenhouse gases is evident.

Significance testing of differences in PDFs. We utilize a Monte Carlo simulation approach to understand the significance of the difference plot (Fig. 6b) between the PDFs of the CMIP6 SLPa downwelling indices for the periods 2000–2100 minus 1850–1950. Here's the process:

1. *Model fitting*: We first fit an AR-1 model to each model's SLPa Downwelling Index time series from 1850-2100 for all 27 models.
2. *Random realizations*: Using the AR-1 process, we generate random realizations of each model's index, resulting in 27 sets of synthetic data.
3. *PDF recalculation*: We recompute the PDFs of the SLPa Downwelling Index for the periods 1850–1950 and 2000–2100 using these random realizations and then calculate their differences, as shown in Fig. 6b.
4. *Repetition and confidence limits*: This process is repeated 10,000 times to generate a large number of realizations of the difference between the PDFs. Using these realizations, we estimate the 95% and 99% confidence intervals of the random differences and plot the confidence curves (Fig. 6b, grey dotted lines).

For example, considering upwelling events with a −2 standard deviation value, the realizations obtained from step 4 provide a PDF of the expected difference from random occurrences, allowing us to establish a confidence limit. Note that these confidence limits vary for each value on the x-axis in Fig. 6b. This variation reflects that differences in counts between the periods 1850–1950 and 2000–2100 are larger for small events (e.g., standard deviations between [−1, 1]) and become smaller as we transition to extreme events (e.g., standard deviations larger than ±2).

Reporting summary

Further information on research design is available in the Nature Portfolio Reporting Summary linked to this article.

Data availability

All datasets used in this study are publicly available online: (1) sea level and surface geostrophic currents data from the Global Ocean Gridded L 4 Sea Surface Heights by Copernicus Marine Data https://doi.org/10.48670/moi-00148, (2) sea surface temperature from the National Centers for Environmental Information 1/4 Degree Daily Optimum Interpolation Sea Surface Temperature Analysis, Version 2.1, between 1982 and 2023, https://psl.noaa.gov/data/gridded/data.noaa.oisst.v2.highres.html, (3) sea level pressure data from the 'NCEP-NCAR Reanalysis 1 at monthly resolution and with a horizontal resolution of 2.5 degrees[58] https://psl.noaa.gov/data/gridded/data.ncep.reanalysis.html, and (4) satellite observations of chlorophyll-a from the Ocean Color CCI Level-3 from 1997 to 2023[59] https://www.oceancolour.org/. Coupled Model Intercomparison Project version 6 data was downloaded from the Program for Climate Model Diagnosis & Intercomparison https://pcmdi.llnl.gov. A copy of the pre-processed data is also available in the code repository GitHib in the code availability section.

Code availability

All the codes and a local copy of the data used this study are available via GitHub: https://github.com/manuocean/rallu.commsenv.nature.2024. All analyses were performed using MATLAB R2021a.

References

1. Bond, N. A., Cronin, M. F., Freeland, H. & Mantua, N. Causes and impacts of the 2014 warm anomaly in the NE Pacific. *Geophys. Res. Lett.* **42**, 3414–3420 (2015).
2. Di Lorenzo, E. & Mantua, N. Multi-year persistence of the 2014/15 North Pacific marine heatwave. *Nat. Clim. Chang.* **6**, 1042 (2016).
3. Amaya, D. J., Miller, A. J., Xie, S. P. & Kosaka, Y. Physical drivers of the summer 2019 North Pacific marine heatwave. *Nat. Commun.* **11**, 9 (2020).
4. Xu, T. T., Newman, M., Capotondi, A. & Di Lorenzo, E. The continuum of Northeast Pacific marine heatwaves and their relationship to the Tropical Pacific. *Geophys. Res. Lett.* **48**, 10 (2021).
5. Di Lorenzo, E. et al. Modes and mechanisms of Pacific decadal-scale variability. *Annu. Rev. Mar. Sci.* **15**, 249–275 (2023).
6. NOAA, N. O. a. A. A. *NOAA Fisheries Mobilizes to Gauge Unprecedented West Coast Toxic Algal Bloom*. (2016).
7. NOAA, N. O. a. A. A. *2015 Large whale Unusual Mortality Event in the Western Gulf of Alaska*. (2016).
8. NOAA, N. O. a. A. A. *2013–2016 California Sea Lion Unusual Mortality Event in California*. (2016).
9. Jones, T. et al. Massive mortality of a planktivorous seabird in response to a marine heatwave. *Geophys. Res. Lett.* **45**, 3193–3202 (2018).
10. McCabe, R. M. et al. An unprecedented coastwide toxic algal bloom linked to anomalous ocean conditions. *Geophys. Res. Lett.* **43**, 10366–10376 (2016).
11. Piatt, J. F. et al. Extreme mortality and reproductive failure of common murres resulting from the northeast Pacific marine heatwave of 2014-2016. *PLoS One* **15**, 32 (2020).
12. Batten, S. D., Ostle, C., Hélaouët, P. & Walne, A. W. Responses of Gulf of Alaska plankton communities to a marine heat wave. *Deep-Sea Res. Part II-Top. Stud. Oceanogr.* **195**, 9 (2022).
13. Barbeaux, S. J., Holsman, K. & Zador, S. Marine heatwave stress test of ecosystem-based fisheries management in the Gulf of Alaska Pacific Cod. *Front. Mar. Sci.* **7**, 21 (2020).
14. Suryan, R. M. et al. Ecosystem response persists after a prolonged marine heatwave. *Sci. Rep.* **11**, 17 (2021).
15. Yang, Q. et al. How "The Blob" affected groundfish distributions in the Gulf of Alaska. *Fish. Oceanogr.* **28**, 434–453 (2019).
16. Welch, H. et al. Impacts of marine heatwaves on top predator distributions are variable but predictable. *Nat. Commun.* **14**, 5188 (2023).
17. Hauri, C. et al. More than marine heatwaves: a new regime of heat, acidity, and low oxygen compound extreme events in the Gulf of Alaska. *AGU Adv.* **5**, 18 (2024).
18. Athanase, M., Sanchez-Benitez, A., Goessling, H. F., Pithan, F. & Jung, T. M. Projected amplification of summer marine heatwaves in a warming Northeast Pacific Ocean. *Commun. Earth Environ.* **5**, 12 (2024).
19. Di Lorenzo, E. et al. Synthesis of Pacific Ocean climate and ecosystem dynamics. *Oceanography* **26**, 68–81 (2013).
20. Ueno, H. et al. Review of oceanic mesoscale processes in the North Pacific: physical and biogeochemical impacts. *Prog. Oceanogr.* **212**, 37 (2023).
21. Johnson, W. K., Miller, L. A., Sutherland, N. E. & Wong, C. S. Iron transport by mesoscale Haida eddies in the Gulf of Alaska. *Deep-Sea Res. Part II-Top. Stud. Oceanogr.* **52**, 933–953 (2005).
22. Ladd, C. et al. A synoptic survey of young mesoscale eddies in the Eastern Gulf of Alaska. *Deep-Sea Res. Part II-Top. Stud. Oceanogr.* **56**, 2460–2473 (2009).
23. Ladd, C. Interannual variability of the Gulf of Alaska eddy field. *Geophys. Res. Lett.* **34**, 5 (2007).

24. Lippiatt, S. M., Lohan, M. C. & Bruland, K. W. The distribution of reactive iron in northern Gulf of Alaska coastal waters. *Mar. Chem.* **121**, 187–199 (2010).

25. Rosengard, S. Z., Freshwater, C., McKinnell, S., Xu, Y. & Tortell, P. D. Covariability of Fraser River sockeye salmon productivity and phytoplankton biomass in the Gulf of Alaska. *Fish. Oceanogr.* **30**, 666–678 (2021).

26. Crawford, W. R., Brickley, P. J., Peterson, T. D. & Thomas, A. C. Impact of Haida Eddies on chlorophyll distribution in the Eastern Gulf of Alaska. *Deep-Sea Res. Part II-Top. Stud. Oceanogr.* **52**, 975–989 (2005).

27. Mackas, D. L. & Galbraith, M. D. Zooplankton distribution and dynamics in a North Pacific eddy of coastal origin: 1. Transport and loss of continental margin species. *J. Oceanogr.* **58**, 725–738 (2002).

28. Mackas, D. L., Tsurumi, M., Galbraith, M. D. & Yelland, D. R. Zooplankton distribution and dynamics in a North Pacific Eddy of coastal origin: II. Mechanisms of eddy colonization by and retention of offshore species. *Deep-Sea Res. Part II-Top. Stud. Oceanogr.* **52**, 1011–1035 (2005).

29. Atwood, E., Duffy-Anderson, J. T., Horne, J. K. & Ladd, C. Influence of mesoscale eddies on ichthyoplankton assemblages in the Gulf of Alaska. *Fish. Oceanogr.* **19**, 493–507 (2010).

30. Paredes, R. et al. Foraging responses of black-legged kittiwakes to prolonged food-shortages around colonies on the Bering Sea Shelf. *PLoS One* **9**, 15 (2014).

31. Pelland, N. A., Eriksen, C. C. & Lee, C. M. Subthermocline eddies over the Washington Continental Slope as observed by seagliders, 2003-09. *J. Phys. Oceanogr.* **43**, 2025–2053 (2013).

32. Ream, R. R., Sterling, J. T. & Loughlin, T. R. Oceanographic features related to northern fur seal migratory movements. *Deep-Sea Res. Part II-Top. Stud. Oceanogr.* **52**, 823–843 (2005).

33. Santora, J. A. et al. Biogeography of seabirds within a high-latitude ecosystem: use of a data-assimilative ocean model to assess impacts of mesoscale oceanography. *J. Mar. Syst.* **178**, 38–51 (2018).

34. Chen, H. H. et al. Combined oceanic and atmospheric forcing of the 2013/14 marine heatwave in the northeast Pacific. *NPJ Clim. Atmos. Sci.* **6**, 10 (2023).

35. Stabeno, P. J. et al. Meteorology and oceanography of the Northern Gulf of Alaska. *Cont. Shelf Res.* **24**, 859–897 (2004).

36. Crawford, W. R., Cherniawsky, J. Y. & Foreman, M. G. G. Multi-year meanders and eddies in the Alaskan Stream as observed by TOPEX/Poseidon altimeter. *Geophys. Res. Lett.* **27**, 1025–1028 (2000).

37. Di Lorenzo, E., Foreman, M. G. G. & Crawford, W. R. Modelling the generation of Haida Eddies. *Deep-Sea Res. Part II-Top. Stud. Oceanogr.* **52**, 853–873 (2005).

38. Henson, S. A. & Thomas, A. C. A census of oceanic anticyclonic eddies in the Gulf of Alaska. *Deep-Sea Res. Part I-Oceanogr. Res. Pap.* **55**, 163–176 (2008).

39. Ladd, C., Kachel, N. B., Mordy, C. W. & Stabeno, P. J. Observations from a Yakutat eddy in the northern Gulf of Alaska. *J. Geophys. Res. -Oceans* **110**, 11 (2005).

40. Whitney, F. & Robert, M. Structure of Haida eddies and their transport of nutrient from coastal margins into the NE Pacific Ocean. *J. Oceanogr.* **58**, 715–723 (2002).

41. Combes, V., Di Lorenzo, E. & Curchitser, E. Interannual and decadal variations in cross-shelf transport in the Gulf of Alaska. *J. Phys. Oceanogr.* **39**, 1050–1059 (2009).

42. Crawford, W. R. Physical characteristics of Haida Eddies. *J. Oceanogr.* **58**, 703–713 (2002).

43. Cheng, Y. H., Ho, C. R., Zheng, Q. N. & Kuo, N. J. Statistical characteristics of mesoscale eddies in the North Pacific derived from satellite Altimetry. *Remote Sens.* **6**, 5164–5183 (2014).

44. Crawford, W. R., Brickley, P. J. & Thomas, A. C. Mesoscale eddies dominate surface phytoplankton in Northern Gulf of Alaska. *Prog. Oceanogr.* **75**, 287–303 (2007).

45. Martínez-Moreno, J. et al. Global changes in oceanic mesoscale currents over the satellite altimetry record. *Nat. Clim. Chang.* **11**, 397 (2021).

46. Beech, N. et al. Long-term evolution of ocean eddy activity in a warming world. *Nat. Clim. Chang.* **12**, 910 (2022).

47. Deser, C., Phillips, A. S., Alexander, M. A. & Smoliak, B. V. Projecting North American climate over the next 50 years: uncertainty due to internal variability. *J. Clim.* **27**, 2271–96 (2014).

48. Giamalaki, K. et al. Future intensification of extreme Aleutian low events and their climate impacts. *Sci. Rep.* **11**, 12 (2021).

49. Gan, B. L. et al. On the response of the Aleutian low to greenhouse warming. *J. Clim.* **30**, 3907–3925 (2017).

50. Screen, J. A. et al. Consistency and discrepancy in the atmospheric response to Arctic sea-ice loss across climate models. *Nat. Geosci.* **11**, 155 (2018).

51. Cohen, J. et al. Recent Arctic amplification and extreme mid-latitude weather. *Nat. Geosci.* **7**, 627–637 (2014).

52. Woollings, T., Gregory, J. M., Pinto, J. G., Reyers, M. & Brayshaw, D. J. Response of the North Atlantic storm track to climate change shaped by ocean–atmosphere coupling. *Nat. Geosci.* **5**, 313–317 (2012).

53. Song, S. Y., Yeh, S. W., Kim, H. & Holbrook, N. J. Arctic warming contributes to increase in Northeast Pacific marine heatwave days over the past decades. *Commun. Earth Environ.* **4**, 9 (2023).

54. Blackport, R. & Screen, J. A. Insignificant effect of Arctic amplification on the amplitude of midlatitude atmospheric waves. *Sci. Adv.* **6**, 9 (2020).

55. Cohen, J. et al. Divergent consensuses on Arctic amplification influence on midlatitude severe winter weather. *Nat. Clim. Chang.* **10**, 20 (2020).

56. Kennel, C. F. & Yulaeva, E. Influence of Arctic sea-ice variability on Pacific trade winds. *Proc. Natl Acad. Sci. USA* **117**, 2824–2834 (2020).

57. Furtado, J. C., Di Lorenzo, E., Schneider, N. & Bond, N. A. North Pacific decadal variability and climate change in the IPCC AR4 models. *J. Clim.* **24**, 3049–3067 (2011).

58. Kalnay, E. et al. The NCEP/NCAR 40-year reanalysis project. *Bull. Am. Meteorol. Soc.* **77**, 437–471 (1996).

59. Sathyendranath, S. et al. An ocean-colour time series for use in climate studies: the experience of the ocean-colour climate change initiative (OC-CCI). *Sensors* **19**, 31 (2019).

60. Cummins, P. F. & Lagerloef, G. S. E. Wind-driven interannual variability over the northeast Pacific Ocean. *Deep Sea Res. Part I* **51**, 2105–2121 (2004).

61. Chhak, K. C., Di Lorenzo, E., Schneider, N. & Cummins, P. F. Forcing of low-frequency ocean variability in the Northeast Pacific. *J. Clim.* **22**, 1255–1276 (2009).

62. Di Lorenzo, E., Mountain, D., Batchelder, H. P., Bond, N. & Hofmann, E. E. Advances in marine ecosystem dynamics from US GLOBEC the horizontal-advection bottom-up forcing paradigm. *Oceanography* **26**, 22–33 (2013).

63. Schneider, N. & Cornuelle, B. D. The forcing of the Pacific decadal oscillation. *J. Clim.* **18**, 4355–4373 (2005).

64. Lee, J. Y. et al. *Future Global Climate: Scenario-Based Projections and Near-Term Information. Climate Change 2021: The Physical Science Basis. Contribution of Working Group I to the Sixth Assessment Report of the Intergovernmental Panel on Climate Change*. (Cambridge University Press, 2021).

Acknowledgements

Author contributions

M.C.R. and C.M.K. equally contributed to all aspects of the manuscript. E.D.L. contributed to the design of the research and assisted with analyses, discussion, and manuscript writing.

Competing interests

The authors declare no competing interests.

Additional information

Supplementary information The online version contains supplementary material available at https://doi.org/10.1038/s43247-024-01785-x.

Correspondence and requests for materials should be addressed to Emanuele Di Lorenzo.

Peer review information *Communications Earth & Environment* thanks Hiromichi Ueno, Yuntao Wang, and the other, anonymous, reviewer(s) for their contribution to the peer review of this work. Primary Handling Editor: Alireza Bahadori. A peer review file is available.

Reprints and permissions information is available at http://www.nature.com/reprints

Publisher's note Springer Nature remains neutral with regard to jurisdictional claims in published maps and institutional affiliations.